Available online at www.sciencedirect.com
ScienceDirect
Geochimica et Cosmochimica Acta 74 (2010) 187–202
Geochimica et Cosmochimica Acta
www.elsevier.com/locate/gca

Uranium-rich opal from the Nopal I uranium deposit, Peña Blanca, Mexico: Evidence for the uptake and retardation of radionuclides

Michael Schindler *, Mostafa Fayek, Frank C. Hawthorne

Department of Geological Sciences, University of Manitoba, Winnipeg, Man., Canada R3T2N2

Received 20 January 2009; accepted in revised form 16 September 2009; available online 22 September 2009

Abstract

The Nopal I uranium deposit of the Sierra Peña Blanca, Mexico, has been the focus of numerous studies because of its economic importance and its use as a natural analog for nuclear-waste disposal in volcanic tuff. Secondary uranyl minerals such as uranophane, $Ca[(UO_2)(SiO_3OH)]_2(H_2O)_5$, and weeksite, $(K,Na)_2[(UO_2)_2(Si_5O_{13})](H_2O)_3$, occur in the vadose zone of the deposit and are overgrown by silica glaze. These glazes consist mainly of opal A, which contains small particles of uraninite, UO_2, and weeksite. Close to a fault between brecciated volcanic rocks and welded tuff, a greenish silica glaze coats the altered breccia. Yellow silica glazes from the center of the breccia pipe and from the high-grade pile coat uranyl-silicates, predominantly uranophane and weeksite. All silica glazes are strongly zoned with respect to U and Ca, and the distribution of these elements indicates curved features and spherical particles inside the coatings. The concentrations of U and Ca correlate in the different zones and both elements inversely correlate with the concentration of Si. Zones within the silica glazes contain U and Ca in a 1:1 ratio with maximum concentrations of 0.08 and 0.15 at.% for the greenish and yellow glazes, respectively, suggesting trapping of either Ca_1U_1-aqueous species or -particles in the colloidal silica. X-ray photoelectron spectroscopy (XPS), Fourier-transform infra-red spectroscopy (FTIR), and oxygen-isotope ratios measured by secondary-ion mass spectrometry (SIMS) indicate higher U^{6+}/U^{4+} ratios, higher proportions of Si–OH groups and lower $\delta^{18}O$ values for the greenish silica glaze than for the yellow silica glaze. These differences in composition reflect increasing brecciation, porosity, and permeability from the center of the breccia pipe (yellow silica glaze) toward the fault (green silica glaze), where the seepage of meteoric water and Eh are higher.

1. INTRODUCTION

The recent decision to discard Yucca Mountain in southern Nevada as a potential site for the repository of high-level nuclear waste (Long and Ewing, 2004; MacFarlane and Ewing, 2006; Ewing and von Hippel, 2009) leaves open questions about future potential sites for high-level nuclear waste in the US. Potential sites may occur in various geological media such as granite, shale, salt, and volcanic tuff. Numerous studies on the volcanic tuff at Yucca Mountain showed that calcite and amorphous silica (opal) are the dominant secondary minerals within fractures and that these secondary minerals formed during evaporation of meteoric water (e.g. Szabo and Kyser, 1990; Paces et al., 2001; Whelan et al., 2002). Precipitation of amorphous silica may also occur where solutions are mobilized through heat generated by nuclear waste inside a repository. Laboratory experiment and numerical simulation on mineral dissolution and precipitation in the volcanic tuffs (Dobson et al., 2003) indicate flow of water through the tuff at 80 °C that resulted in the precipitation of amorphous silica, sealing most of the fractures inside the tuff unit within

* Corresponding author. Present address: Department of Earth Sciences, Laurentian University, Sudbury, ON, Canada P3E 2C6. Tel.: +1 705 675 1151/2365.
E-mail address: mschindler@laurentian.ca (M. Schindler).

0016-7037/$ - see front matter © 2009 Elsevier Ltd. All rights reserved.
doi:10.1016/j.gca.2009.09.017

5 days. These studies indicate that calcite and amorphous silica (opal) are the dominant secondary phases, which would form in geological and climatic settings similar to that of Yucca Mountain.

Once released from nuclear-waste containers, radionuclides could either adsorb or co-precipitate with both minerals. Adsorption and co-precipitation of $(UO_2)^{2+}$ with calcite and the formation of secondary U-minerals on the surface of calcite have been investigated in numerous studies (e.g. Reeder et al., 2001; Schindler et al., 2004). There has been work on the interaction of $(UO_2)^{2+}$ with silicic acid in aqueous solution (Moll et al., 1998) and its adsorption onto colloidal silica (e.g. Michard et al., 1996; Reich et al., 1998). However no work has been done on the speciation of U in opal, a feature that is critical to our understanding of

(a) the trapping of U during the gelation of silicic acid to form colloidal silica;
(b) the incorporation of U into opal during hardening of the colloidal silica;
(c) immobilization of U by opal over a longer (geological) time.

U-bearing opals can occur on the surface of exposed rocks and as fillings in fractures and cavities in the vadose zone of uranium deposits. For example, a thin layer of opal coats minerals and rocks at the exposed part of the vadose zone of the U ore deposit Nopal I at Peña Blanca, Mexico, (Cesbron et al., 1993). These thin layers of opal are commonly referred to as silica glaze and form a more or less continuous coating on many exposed rocks and minerals at the Earth's surface (Dorn, 1998). In contrast, opals formed in the subsurface at Yucca Mountain and Nopal I commonly occur as fillings in fractures, pores, and cavities, and form a discontinuous coating on coarse crystal aggregates of chalcedony, quartz, calcite, and Fe-oxides (e.g. Whelan et al., 2002; Dobson et al., 2008).

The goal of this study is to mineralogically, chemically, and isotopically characterize U-bearing silica glazes from the vadose zone of the uranium ore deposit at Nopal I. We will use the terms *opaline coating* for coatings formed in pores and fractures at the subsurface and *silica glaze* for coatings formed on exposed rocks in the vadose zone. The term *opal* will be used when discussing specific properties of the mineral.

1.1. Occurrence of silica glazes in arid settings

Silica glazes are common in arid and semi-arid regions and their formation on exposed rock surfaces is accelerated in regions of low precipitation (Dorn, 1998; Perry et al., 2006 and references therein). They can occur as thin, colourless, transparent, highly lustrous coatings that are also described as desert glaze. Silica glazes vary in appearance and chemical composition; they can contain large amounts of detrital material and up to 30 and 40 wt.% Al_2O_3 and FeO, respectively (Dorn, 1998). Desert varnish is a silica-rich coating with significant amounts of Fe, Mn, and organic material. On the basis of trace-metal ratios (Y/Ho and Ce/La), Thiagarajan and Lee (2004) showed that the components inside the varnish originates from external sources (i.e. windborne particles) rather than from the underlying rock. Similarly, Curtiss et al. (1985) argued that silica glaze from the dry-lands of Hawaii forms through an abiotic solution-deposition process in which particulate matter on the rock surface partly dissolves in water films formed as a result of light rain, dew or fog. Rapid evaporation of the water film on the rock surface favours formation of colloidal material and gels rather than well-ordered crystalline material. The colloidal silica eventually dries and dehydrates at rock-surface temperatures of ~60 °C or higher. Shrinking and drying during the transformation of colloidal silica to silica glaze causes local curvature and partly sintered assemblages of spheres and multilayers (Van Damme, 2000), a possible explanation for the botryoidal morphology of silica glaze (Perry et al., 2006).

1.2. Geological considerations of the uranium ore deposit of Nopal I, Peña Blanca

The volcanic-hosted uranium deposit of Nopal I, Peña Blanca, is a natural analog for the formerly proposed high-level nuclear-waste repository at Yucca Mountain, Nevada (Ildefonse et al., 1990; Muller et al., 1990; Petit, 1990; Pearcy et al., 1994a,b, 1995; Prikryl et al., 1997; Murphy, 2000; Calas et al., 2008). Both sites are located in semi-arid regions and are embedded in Tertiary rhyolitic ash-flow tuffs overlying carbonate rocks within an unsaturated zone (Fig. 1a).

The Nopal I uranium deposit is hosted by brecciated Nopal (44 Ma) and Coloradas rhyolitic ash-flow tuffs. These two units overlie the Pozos conglomerate and Cretaceous limestone. The dimensions of the Nopal I deposit at the ground surface are ~25 by ~70 m, and it extends downward about 90 m; the base of the deposit is about 130 m above the water table. Two dominant fault and fracture systems bound the southwestern and eastern margins of the deposit (Fayek et al., 2006). The southwestern fault is nearly vertical and strikes 305°, and slickensides on the fault surface dip 20°. The fracture system that bounds the eastern margin of the deposit strikes ~350° and shows very little vertical or horizontal movement. A third fault system is exposed along the +10 level (the top) of the deposit. This fault is subhorizontal with a dip of ~20° to the west, and has slickensides that trend 260°. The southwest and east-bounding fault and fracture systems occur throughout the Nopal I deposit and appear to have channeled subsequent hydrothermal fluid flow which resulted in the formation of the breccia pipe that currently hosts the uranium ore. Detailed mapping of the Nopal I deposit shows that brecciation intensifies toward the south where the west- and east-bounding fault and fracture systems intersect. Movement along the southwest-bounding fault seems to have increased brecciation, which in turn enhanced permeability. As a result, the deposit is zoned, with increasing oxidation toward the southern part. Other minor and younger fault and fracture systems (e.g. the E–W fracture system described by Pearcy et al., 1994a,b) also occur throughout the deposit. These younger fracture systems appear open and permeable

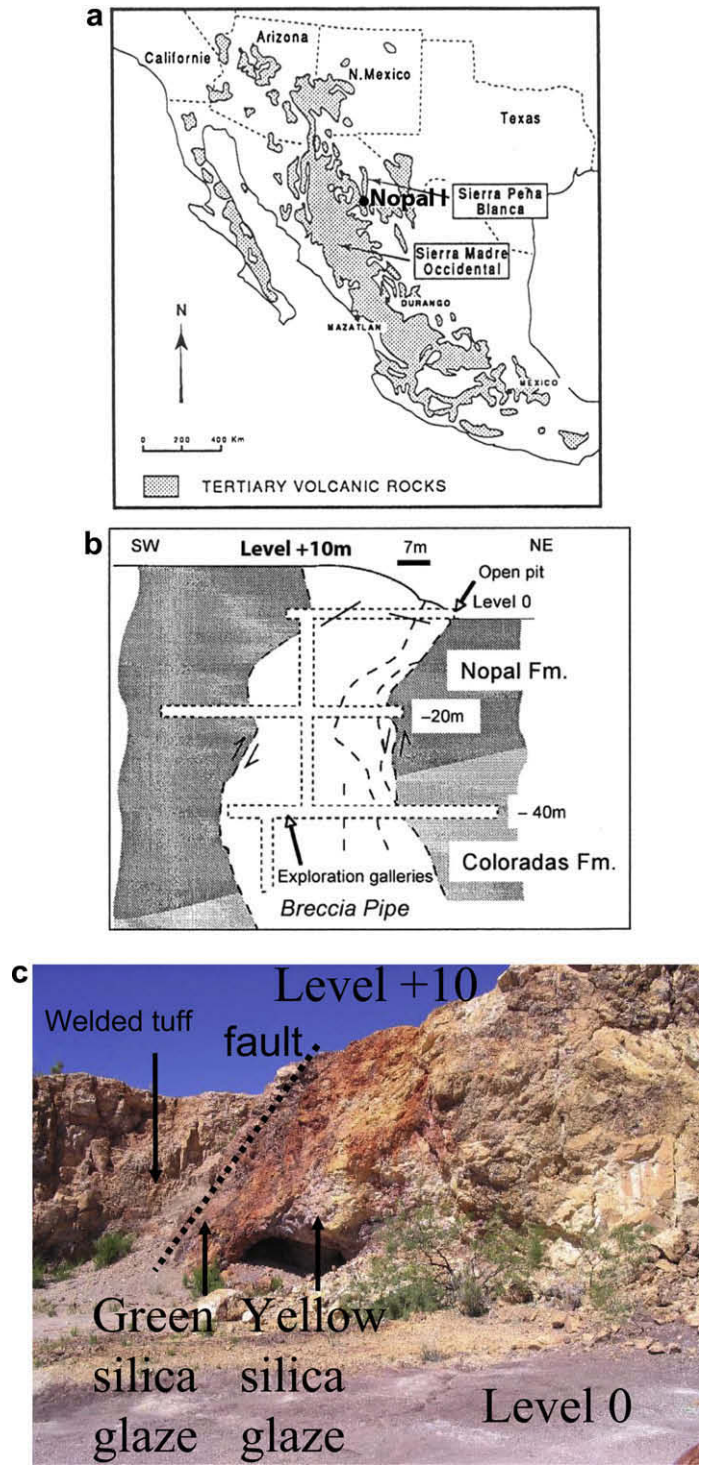

Fig. 1. (a) Geological setting of the Nopal I uranium deposit in the Sierra Peña Blanca, Chihuahua, Mexico (modified from Cesbron, 1993); (b) vertical section of the breccia pipe of the Nopal I deposit (modified from Calas et al. (2008)); (c) photo of the open pit of the breccia pipe; locations of the sampled silica glazes are indicated.

to meteoric fluids and the fractures are lined with secondary U^{6+} minerals where they intersect the main ore body.

The ore body is primarily a breccia zone that contains uraninite in association with pyrite and secondary uranyl minerals (Calas, 1977). Uraninite occurs as dense and massive black cores with an alteration crust of soddyite, $[(UO_2)_2(SiO_4)(H_2O)_2]$, uranophane, $Ca[(UO_2)(SiO_3OH)]_2(H_2O)_5$, and becquerelite, $Ca[(UO_2)_3O_2(OH)_3]_2(H_2O)_8$ (Ildefonse et al., 1990). Other secondary uranyl minerals such as uranophane-β, $Ca[(UO_2)(SiO_3OH)]_2(H_2O)_5$, weeksite,

$(K_xNa_{1-x})_2[(UO_2)_2(Si_5O_{13})](H_2O)_3$, boldwoodite, (K, Na) $[(UO_2)(SiO_3OH)]_2(H_2O)_{1.5}$ and carnotite, $K_2[(UO_2)_2(V_2O_8)](H_2O)_3$, occur along fractures. Here, K-rich minerals (weeksite, boldwoodite, and carnotite) occur in the center of the pipe and the calcic uranyl-silicate uranophane is located in the periphery (Pearcy et al., 1994a,b). All uranyl phases can be overgrown by paragenetically late uranophane-β and coated by silica glaze (Cesbron et al., 1993). A detailed description of the occurrence and paragenesis of the secondary uranyl minerals in the weathered zone of the Nopal I deposit is given by Pearcy et al. (1994a,b). In addition to the Nopal I uranium deposit, uranium mining throughout the Sierra Peña Blanca has resulted in a stock-pile of high-grade ore ~2 km NW of the Nopal I deposit. This stock-pile consists of U-rich boulders that range in size from a few centimeters to several meters.

2. EXPERIMENTAL

2.1. Sampling and sample preparation

Silica glazes of botryoidal morphology were sampled from the high-grade pile and from breccia surfaces between the +10 level and the +0 level at the Nopal I mine site (Fig. 1b and c) and on U-rich boulders from the high-grade pile.

Cross-sections of the coating were embedded in epoxy discs and polished with a mixture of diamond paste and oil emulsion. The polished discs were subsequently washed with ethanol and distilled water, dried in air, and immediately transferred to an X-ray photoelectron spectrometer.

2.2. X-ray photoelectron spectroscopy

The near-surface chemical compositions of the rock coatings were characterized with a Kratos Axis Ultra X-ray photoelectron spectrometer (XPS) equipped with a magnetic-confinement charge-compensation system. The advantages of this system for insulators (e.g. uranyl minerals) have been described in detail by Schindler et al. (2009a,b). Spectra of the U 4f, O 1s, Si 2p, Ca 2p, N 1s, and Fe 3d electrons were collected in high-resolution using monochromatic Al Kα radiation (1486.6 eV) and the charge-compensation system. Spectra were recorded using 20 sweeps, scan rates per sweep of 200 ms with analyzer pass energies of 10 eV (Si 2p) and 160 eV (U 4f), small and large spot sizes and with an aperture size of 110 μm. Resolution for the different pass energies, spot sizes, and aperture are listed in detail in Schindler et al. (2009a,b) and their effect on the FWHM values (FWHM = full-width at half maximum) of the U 4f peaks is described below. Shirley background corrections (Shirley, 1972) and Gaussian–Lorentzian peak shapes of 60 ± 10% were used to fit the U 4f spectra. We also measured Si 2p spectra for synthetic silicic acid (Sigma) and several silicates: opal-CT, α-quartz, and forsterite. The latter specimens were obtained from the mineral collection of the Department of Geological Sciences, University of Manitoba.

The electrostatic sample-charging (which was not completely compensated by the charge neutralizer) was corrected by setting the binding energy of the C 1s electrons of adventitious C–H species on the sample surface equal to 285 eV (Wagner et al., 1979, Handbook of X-ray photoelectron spectroscopy). We use the word *band* to indicate a specific fitted component of the envelope of the U 4f peak, and we use the word *species* to indicate U atoms of different valence and ligancy.

2.3. The U 4f spectra

The presence and relative proportions of $U^{6+}$and U^{4+} were determined by peak fitting of the U $4f_{7/2}$ spectra and examination of the satellite peaks of the U $4f_{5/2}$ peak using the software Vision 2.2.6 (2006). The binding energies and the relative intensities of the bands in the U $4f_{7/2}$ envelope are listed in Table 1. The FWHM values of the bands in the U 4f spectrum vary in the range 1.70–2.00 eV, but were constrained to be equal in each individual spectrum (Table 1). More details on fitting of the U $4f_{7/2}$ spectra and standard deviations of the binding energies and relative proportions of the U-bands are given by Schindler et al. (2009a).

2.4. Electron microprobe analysis and scanning electron microscopy

Chemical compositions of the different types of coatings and element maps for U, Si, Ca, Fe, and Al were measured with a Cameca SX-100 electron microprobe operating in wavelength-dispersion mode with an accelerating voltage of 15 kV, a specimen current of 10 nA, and a beam diameter of 5 μm. The following standards were used: diopside (Ca, Si), UO_2 (U), fayalite (Fe), albite (Na), sanidine (K), and scapolite (Al). Raw intensities were converted to

Table 1
Pass energies (PE), apertures (A), spot size (SP, L = large, S = small), binding energies (BE), full-width at half maximum (FWHM), and proportion (%) of bands in the U $4f_{7/2}$ peak of the rock coatings and weeksite.

Mineral	PE/A/SP	U^{6+} [eV] (BE/FWHM)	[%]	U^{4+} [eV] (BE/FWHM)	[%]	U^{4+} ? [eV] (BE/FWHM)	[%]
Hematite	160/110/S	382.2/1.7	54	380.8/1.7	46	–	
Yellow Opal [a]	160/110/L	381.9/2.0	54	380.3/2.0	29	378.0/ 2.0	7
Yellow Opal [b]	160/110/S	382.3/1.7	56	380.8/1.7	30	379.5/1.7	14
Green Opal	160/110/L	382.4/2.0	68	380.7/2.0	32		
Weeksite	160/55/S	382.4/1.2	83	380.7/1.2	17		

[a] From the center of the breccia pipe at the +3 level.
[b] From the high-grade site at the +10 level.

concentrations using the PAP (Pouchou and Pichoir, 1985) matrix-correction software.

2.5. Infra-red spectroscopy

Fourier-transform infra-red (FTIR) spectra were collected with a Hyperion 2000 spectrometer from Bruker. The spectra of the silica glazes were measured in non-diffuse reflectance mode with a 6 mm aperture in the scan range 4000–600 cm^{-1}. Each spectrum and the corresponding background spectrum of the epoxy disc were scanned 100 times. The spectra were processed with the OPUS v. 4.2 software and transferred in ASCII format to the statistical program Sigma Plot 5.0.

2.6. Secondary-ion mass spectroscopy (SIMS)

Prior to SIMS analysis, the mounts were re-polished and cleaned to remove the carbon coatings and subsequently coated with Au. The mounts were placed in stainless-steel sample holders, and the entire assembly was then placed in the SIMS sample lock and held at high vacuum for a minimum of 8 h prior to the start of the analysis. Oxygen isotopic compositions of standards and uranium minerals were measured with a CAMECA ims 7f secondary-ion mass spectrometer (SIMS) at the University of Manitoba using a Cs^+ primary beam and monitoring O-secondary ions with extreme energy filtering of 200 eV. The ~2 nA primary ion beam was focused to a 10 × 20 μm spot using a 100 μm aperture in the primary column. A Brazil quartz standard with a $\delta^{18}O_{V\text{-}SMOW}$ value of 15.1 ± 0.3‰ was used to correct for IMF. The spot-to-spot reproducibility on the quartz standard was ±0.6‰ (1σ). The overall precision and accuracy for each isotope analysis include errors arising from counting statistics of each individual analysis, calibration to a known standard, and uncertainty in deadtime corrections arising from variable count rates. In general, the overall precision is ±1‰ (2σ). Values are reported in units of ‰ relative to Vienna-standard mean ocean water (V-SMOW).

3. RESULTS

All rock samples were coated with a continuous layer of silica glaze. These glazes were found only on the surface of exposed parts of the vadose zone; i.e. they were not found in the subsurface or in dust-protected parts of the surface (i.e. vertical fractures or cracks), where they could have been formed through evaporation of infiltrated meteoric water. Dorn (1998) showed that silica glazes have many internal fractures which promote their detachment from the underlying rock. This observation suggests that any kind of mining activity would produce either cracks in silica glazes or their complete detachment from the underlying rock. However, silica glazes on the U-rich boulders from the high-grade pile do not display any of these features, which suggests that these glazes were formed after the mining activities at Nopal I.

Rock samples collected from the breccia zone can be distinguished from samples collected elsewhere by the number and thickness of coatings on their surface:

(a) samples from the inner part of the breccia pipe contain kaolinite–hematite and uranyl-mineral coatings overlain by a yellow silica glaze with a maximum thickness of ~500 μm.
(b) samples close to the fault contain thin patches of kaolinite and hematite overlain by a greenish silica glaze with a maximum thickness of ~1 mm.
(c) samples from the high-grade site at the +10 level contain a layer of uranyl minerals overlain by a yellow silica glaze with a maximum thickness of ~1 mm.

3.1. Compositions and spatial distribution of minerals in the coatings

Fig. 2a shows the occurrence of hematite and kaolinite as coatings, replacing feldspar on the surface of a breccia from the center of the breccia pipe. Here, hematite and kaolinte are spatially separated whereas chemical maps also show kaolinite patches overlain by hematite (Figs. 3a–d). Kaolinite also occurs in patches where uranophane, $Ca[(UO_2)(SiO_3OH)]_2(H_2O)_5$, has partly replaced kaolinite. These patches are sandwiched between layers of kaolinite and uranyl minerals and are labeled "transition zone" in Fig. 2a.

The predominant minerals in the coating of secondary uranyl-silicates are uranophane and weeksite, $(K,Na)_2[(UO_2)_2(Si_5O_{13})](H_2O)_3$. Uranophane dominates the inner part of the coating, whereas a mixture of weeksite and uranophane with an average ratio of weeksite:uranophane = 8:1 is present in the outer part of the coating. This layering of uranyl minerals is accompanied by a change in colour and crystal morphology (Fig. 2a and c): massive dark-yellow uranophane is overgrown by pale-yellow fibrous crystals of weeksite. The occurrence of the minerals in the sequence uranophane–(weeksite + uranophane)–opal results in an increase in the ratio of Si:U from the inner to the outer parts of the coating, which is also observed in the chemical maps for both elements and in the variation of the atomic concentration of U as a function of Si (Fig. 4a). The latter plot further indicates small variations in the ratios of Si:U = 1.0(1) in uranophane and U:Si = 0.005(2) in the silica glaze, and larger variations (2.4 ± 0.2) in the layer of weeksite and uranophane (Fig. 4c).

Needle-like crystals of weeksite may be sandwiched between massive precipitates of uranophane and weeksite (Fig. 2a). These crystals are enriched in Na (average composition $K_{1.6}Na_{0.4}[(UO_2)_2(Si_6O_{15})]$) whereas the surrounding weeksite and uranophane are depleted in Na. Small inclusions of a uranyl mineral with a composition similar to becquerelite were also found in these layers (Fig. 3b). Micrometer size particles of weeksite and cubes of uraninite were identified in the silica glaze (Fig. 3e). Fig. 3f shows small fissures filled with becquerelite (identified on the basis of a Ca:U ratio of 1:3) which occur at the interface between the silica glaze and the layer of uranyl-silicates.

Concentrations of U vary in the different types of coatings: silica glazes and hematite coatings contain up to 2.0 and 1.4 wt.% U, respectively (Figs. 2a and 3a). The kaolinite coating overlain by hematite contains only traces of U,

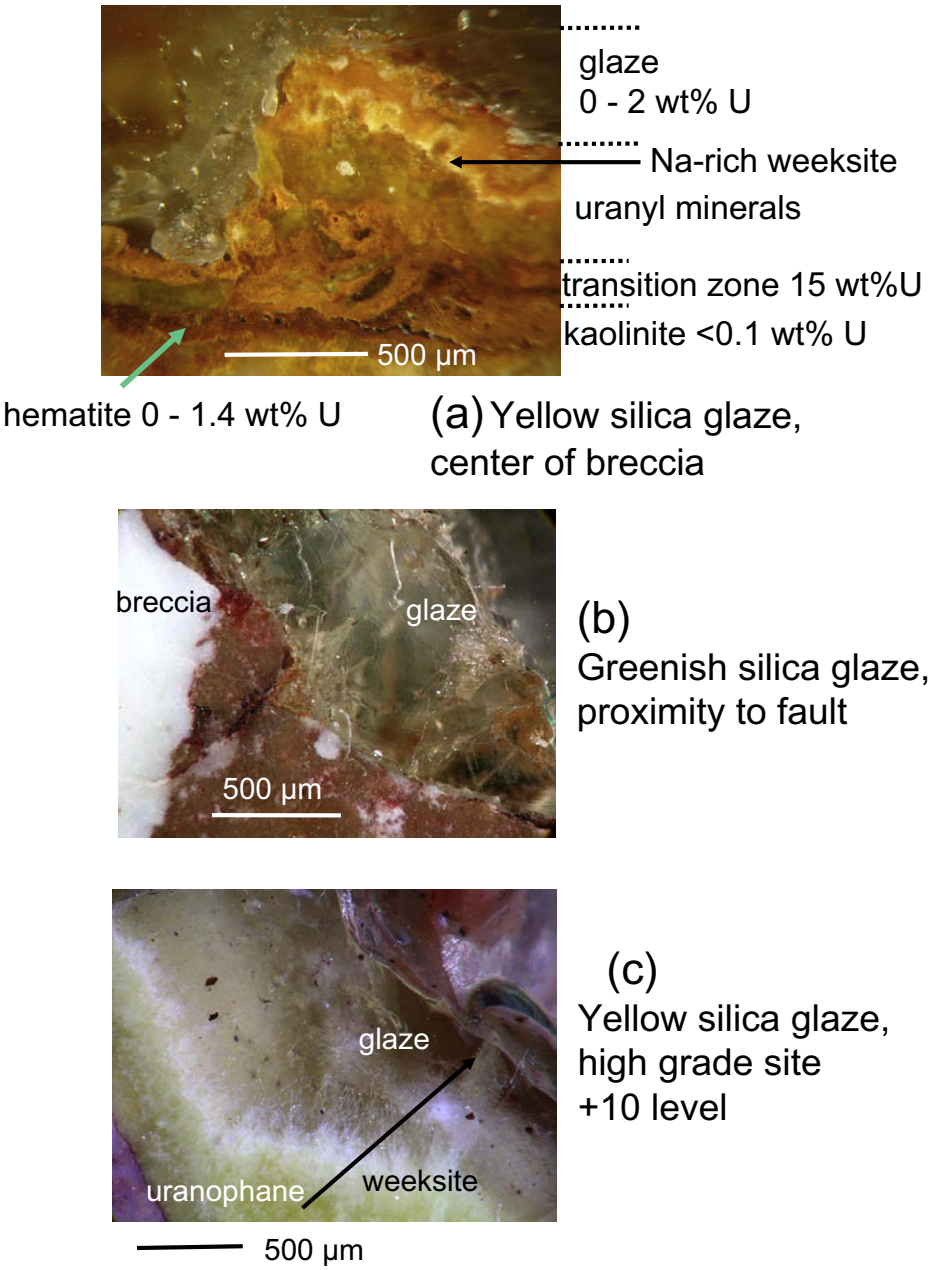

Fig. 2. (a) Photo of a sample from the center of the breccia pipe at the +0 level with a yellow silica glaze overlying layers of uranyl-silicate; various coatings and their U concentration (wt.%) are indicated; (b) greenish silica glaze overlying a breccia with small patches of kaolinite and hematite on the surface; (c) sample from the high-grade site at the +10 level with a yellow silica glaze overlying layers of uranyl-silicates. (For interpretation of the references to colour in this figure legend, the reader is referred to the web version of this paper.)

whereas the transition zones between kaolinite and uranyl minerals contain up to 15 wt.% U (Fig. 2a and 3a). Closer inspection of the chemical maps in Fig. 3a–d also indicates that

(a) parts of the hematite coatings are enriched in Al;
(b) variations in the concentration of U in the layer of uranyl minerals indicate the relative abundance of uranophane, weeksite, uraninite and becquerelite (see below);
(c) low concentrations of Si in the layer of uranyl minerals indicate the presence of uraninite and, most likely, becquerelite;
(d) Al- and Fe-bearing phases occur between the layers of uranyl minerals and the silica glaze.

Electron microprobe analysis of the silica glaze shows that concentrations of common elements such as Al, Fe, Na, K, Mg, S, P, and Ti in the Nopal I deposit are below

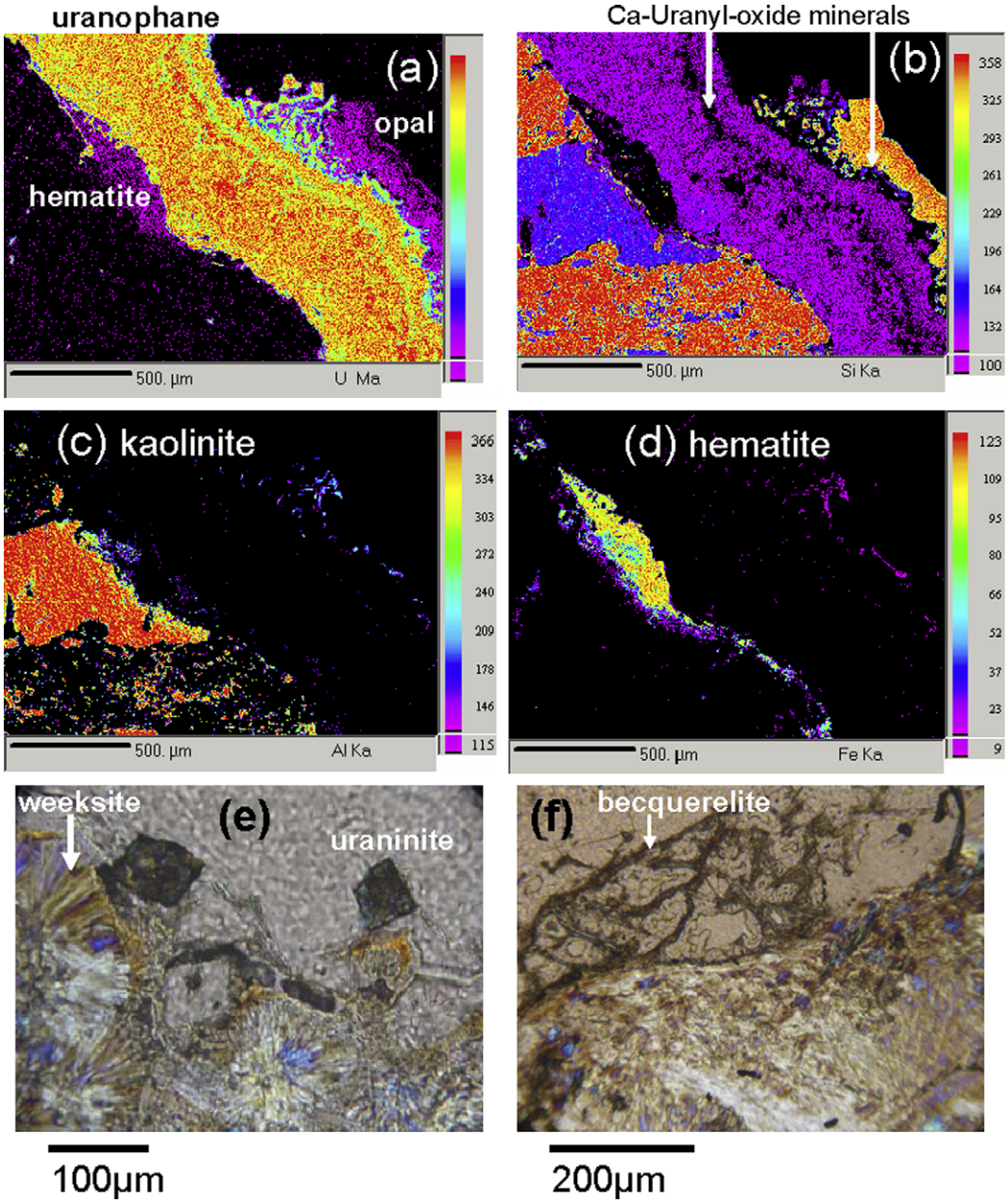

Fig. 3. Chemical maps of (a) U, (b) Si, (c) Al, and (d) Fe for the sample with the yellow silica glaze from the center of the breccia pipe at the +0 level; occurrence of Ca-uranyl oxides (becquerelite), kaolinite, and hematite are indicated; (e and f) optical-microscopy image of a thin section under cross-polarized light, indicating detritus material of uraninite and weeksite (e) and fissures filled with becquerelite (f) inside the silica glaze.

the detection limit of the instrument, and high-resolution scans of the C 1s peak by XPS did not indicate the occurrence of $(CO_3)^{2-}$ groups. The silica glazes are strongly zoned with respect to Si, U, and Ca (Fig. 4b and c). Here, zones can display various geometric forms: circular (Fig. 4b), layered (Fig. 4e), and rectangular to circular (Fig. 4c). The circular and layered zones follow the botryoidal morphology of the silica glazes. Closer inspection of the chemical maps for Si, U, and Ca shows that the concentrations of U and Ca are positively correlated (Fig. 4b) and both are negatively correlated with the concentration of Si (Fig. 4c). The yellow silica glazes contain Ca and U in ~1:1 ratios and with an average concentration of 0.15 at.% (Fig. 4d).

Fig. 4e shows a backscattered-electron image of the greenish silica glaze. Chemical analysis along a traverse perpendicular to the layering also indicates positive correlation between the concentrations of U and Ca and negative correlations between U and Si and Ca and Si. The greenish silica glaze also contains Ca and U in a ratio of ~1:1 but the concentrations (0.08 at.%) of the elements are lower than in the yellow glaze (Fig. 4f).

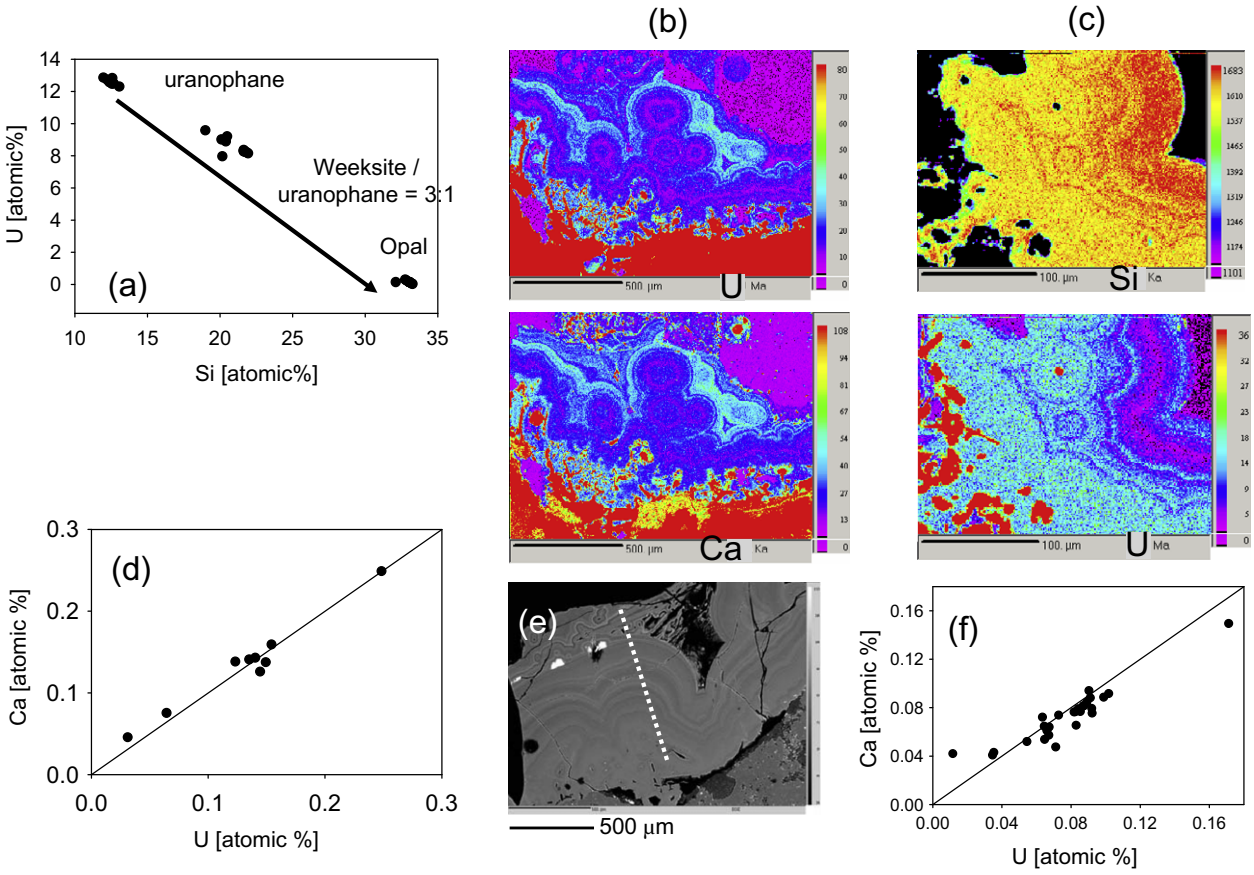

Fig. 4. (a) Plot of the atomic% of Si versus U, indicating distinct U:Si ratios for the minerals in the coatings, arrows in the element maps indicate the sequence of coating from the bottom (uranophane) to the top of the silica glaze; Chemical maps of (b) U and Ca, and (c) U and Si, taken from the sample with the yellow silica glaze from the center of the breccia pipe at the +0 level; (d) plot with the atomic% of U versus Ca in various zones inside the latter silica glaze; a Ca:U ratio of 1:1 is indicated by a solid line; (e) Image taken in backscattering mode of the greenish silica glaze; (f) plot with the atomic% of U versus Ca in different zones of the latter glaze; the U:Ca ratio of 1:1 is indicated by a solid line. For interpretation of the references to colour in this figure legend, the reader is referred to the web version of this paper.

3.2. Valence of U in the coatings

Fig. 5 shows the U $4f_{7/2}$ spectra for the hematite and yellow silica glaze from the center of the breccia pipe and for the greenish silica glaze. All U $4f_{7/2}$ spectra have a prominent maximum at 381.9–382.4 eV and a broad shoulder at 380.0–381.0 eV.

Schindler et al. (2009a) reported typical binding energies for U^{6+} and U^{4+} bands in the U $4f_{7/2}$ peak of 382.0–382.3 and 380.4–380.7 eV for uranophane and uranophane-β and for various uranyl-hydroxy-hydrates without divalent cations, respectively. We additionally measured the U 4f spectrum of weeksite (Fig. 5), which has a higher Si:U ratio (5:2) than uranophane (1:1). Here, the bands for U^{6+} and U^{4+} occur at higher binding energies (382.4 and 380.7 eV) than in the spectra of uranophane, indicating a shift of the U-bands to higher binding energy with the number of silicate polyhedra around U. Note that the satellite peaks for U^{6+} and U^{4+} are not resolved in most of the spectra, a typical feature in U 4f spectra taken from either samples with low concentrations of U or from small U-bearing crystals (Schindler et al., 2009a).

Considering the binding energies for U^{6+} and U^{4+} in U 4f spectra of uranyl minerals, bands below the maximum and the broad shoulder in the U $4f_{7/2}$ spectrum for the hematite and silica glazes were assigned to U^{6+} and U^{4+}. The presence of U^{5+} in the silica glaze samples cannot be ruled out, but resolution of the U 4f peaks and its satellite peaks were not conclusive in term of occurrence and proportion of the U^{5+} bands. An additional U-band at the lower-binding-energy side of the U 4f spectrum (378.4–378.7 eV, Table 1 and Fig. 5) occurs in the spectra of the yellow silica glaze; this band could not be assigned to any known U^{4+} species in U-bearing minerals.

3.3. Structural characterization of the silica glaze by X-ray diffraction

Opal has the general composition $SiO_2 \cdot nH_2O$. Although only opal is recognized as a mineral species, it is commonly subdivided into opal A (A = amorphous) without any short-range order of the silicate tetrahedra, and opal-CT and opal-C (CT = cristobalite–trydimite) with medium-range order of the silicate tetrahedra as six-membered rings

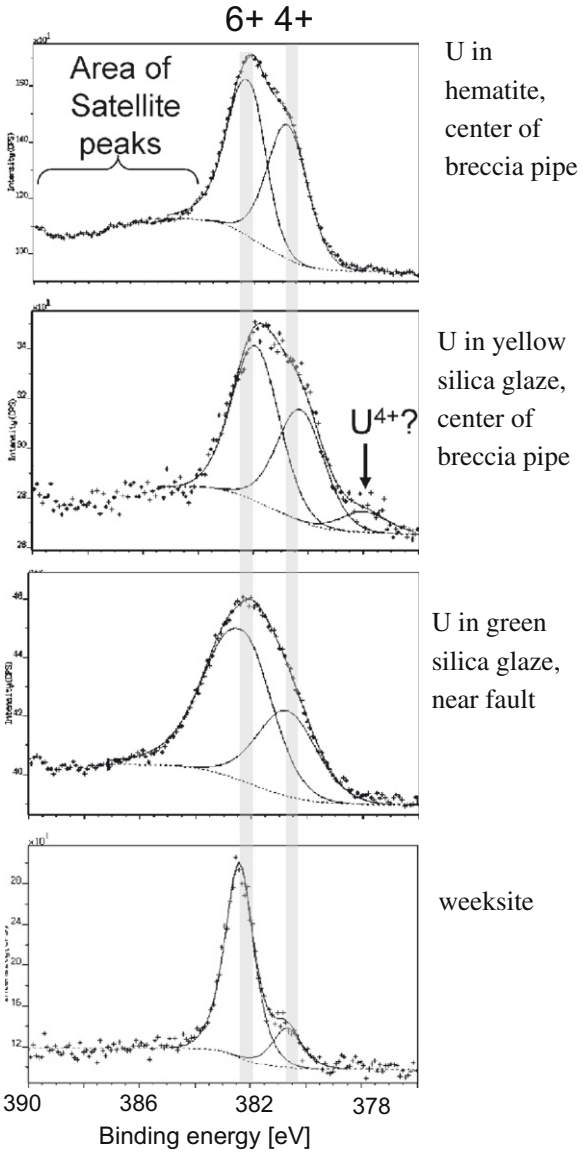

Fig. 5. .The U $4f_{7/2}$ spectra for the silica glazes and weeksite. The location of the $U^{6+}$and U^{4+} bands and their variation in binding energy are indicated with vertical grey-shaded bars.

(Smith, 1998). These opal modifications can be distinguished by X-ray diffraction (XRD) as the location and full-width at half maximum (FWHM) of the peak at 20–23° 2θ (Cu Kα) vary with the degree of short-range order (e.g. Smith, 1998; Herdianita et al., 2000; Lynne and Campbell, 2004). For the transition opal A to opal-CT, Lynne and Campbell (2004) observed a shift in the maximum of the peak from $22.2 \pm 0.15°$ 2θ to $21.7 \pm 0.20°$ 2θ and a decrease in FWHM from $d = 1.30$–1.33 to 0.21–0.33 Å. Furthermore, Lynne et al. (2005) reported a shift of the X-ray diffraction peak with incorporation of Fe into opal A from 22.2° 2θ for Fe-poor samples to 22.6° 2θ for Fe-rich samples. The XRD patterns of all silica glazes from the Nopal I deposit and the high-grade pile show a broad peak from 15 to 35° 2θ with a maximum at $22.6 \pm 0.20°$ 2θ (Cu Kα) and an average FWHM value of $d = 1.5$ Å ± 0.10 (Fig. 6a). The latter two values clearly indicate that all silica glazes are composed of opal A and that, similar to the XRD patterns of Fe-rich samples, the presence of U and Ca in the silica glazes produces a shift of the maximum to higher values of two-theta.

3.4. Structural characterization of silica glaze by X-ray photoelectron spectroscopy

The degree of polymerization of silica tetrahedra in amorphous material can be determined by nuclear magnetic resonance (NMR) spectroscopy, Raman spectroscopy and X-ray photoelectron spectroscopy (XPS). For the latter method, structural differences on the surface of silicates can be explored by examining the binding energies of the Si 2p peak (Si $2p_{3/2}$ and Si $2p_{1/2}$), which shifts to higher energies with an increase in the number of polymerized silicate tetrahedra (Wagner et al., 1979) and with the degree of protonation of the O-atoms of the silica tetrahedra (e.g. Schindler et al., 2009c). For example, Fig. 7a and e show the Si 2p spectra of opal-CT (identified in an XRD pattern) and synthetic silicic acid ($H_2SiO_3 \cdot nH_2O$). Silicic acid has a higher degree of hydration than opal-CT and consequently, the peak in the Si 2p spectra shifts from 103.2 eV in opal-CT to 104.0 eV in silicic acid. Fig. 7d and f show further the Si 2p spectra of quartz, SiO_2, and forsterite, Mg_2SiO_4. The polymerization degree of the silicate tetrahedra is higher in quartz (framework) than forsterite (isolated tetrahedron) and consequently, the peak in the Si 2p spectra shifts from 102 eV in forsterite to 103.2 eV in quartz.

Fig. 7b and c show the Si 2p spectra of silica glazes from the Nopal I deposit. Here, the Si 2p peak of the greenish coating occurs at the same binding energy (104.0 eV) as the Si 2p peak of silicic acid, whereas the peaks of the yellow silica glazes occur at binding energies (103.5–103.6 eV), half way between the peaks for opal-CT and silicic acid. These differences in binding energy suggest that the number of Si-atoms bonding to OH and H_2O groups increases from the yellow glaze to the greenish glaze.

The proportions of OH and H_2O with respect to other O species on the surface can be determined by fitting an O 1s spectrum to bands between 530 and 534 eV (Schindler et al., 2009b). However, surfaces often contain contamination such as adventitious species containing C, N, H, and O. The silica glazes were polished with mixtures of diamond paste and oil emulsion, and subsequently washed with ethanol and distilled water. C 1s and N 1s spectra taken from the silica glazes indicate the presence of *C–N*, *C–O*, and *N–O* species on their surface. The latter O-bearing species overlap with *OH* and *H_2O* bands in an O 1s spectrum and therefore can lead to misinterpretation with respect to the presence and proportions of O species on the surface.

Surface contamination can be removed with acids or with an ion-sputtering system prior to XPS measurement. However, dissolution experiments on uranyl minerals with acidic solutions and sputtering of surfaces containing U and O show that both procedures affect the valence of U and the chemical environments of U and O (Schindler et al., 2009a,b).

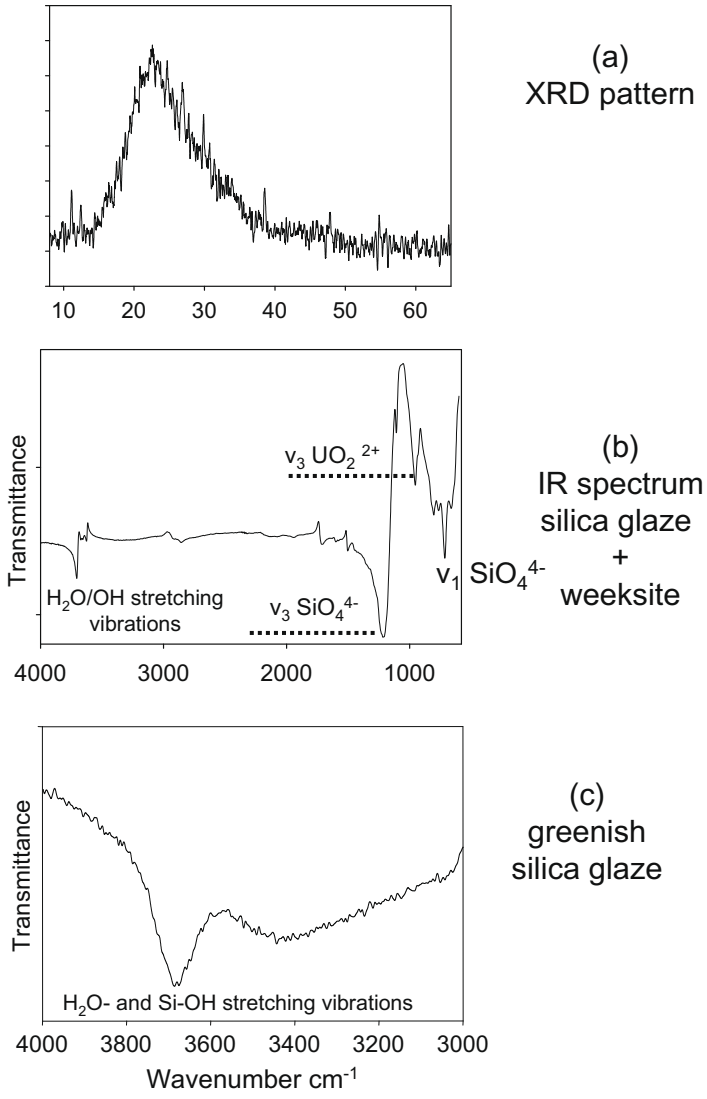

Fig. 6. (a) Typical X-ray diffraction pattern (XRD) for the silica glazes from Nopal; (b and c) FTIR spectra of the silica glaze with weeksite inclusions from the center of the breccia (b) and of the greenish silica glaze (c); vibrations corresponding to prominent bands in the spectra are indicated.

3.5. FTIR-spectroscopy

Fig. 6b shows an FTIR spectrum taken in reflectance mode of the yellow silica glaze from the outer rim, close to the layer of uranyl minerals that contains small inclusion of weeksite crystals. The spectrum shows four prominent bands at 795, 915, 1055, and 3650 cm^{-1} and small bands at 3000–3500 and 1400–2000 cm^{-1}. Vochten et al. (1997) and Cejka (1999) reported IR spectra of synthetic weeksite crystals. They assigned the bands at 795 and 1055 cm^{-1} to the $v1$ symmetric stretching vibration and $v3$ anti-symmetric stretching vibration of the silicate tetrahedron, respectively. Furthermore, they assigned the band at 915 cm^{-1} to the $v3$ anti-symmetric stretching frequency of the UO_2^{2+} ion and the band at 3640 cm^{-1} to vibrations of H_2O groups which are strongly bonded to cations in the structure. Cejka (1999) also showed that the small bands in the regions 1400–2000 and 3000–3500 cm^{-1} correspond to further vibrations of OH and H_2O groups.

Fig. 6c shows a typical FTIR spectrum in the region 3000–4000 cm^{-1} of silica glazes with no visible inclusions of uranyl minerals. The broad band at 3680 cm^{-1} indicates the presence of weakly bonded H_2O groups and Si–OH groups on the surface of the opaline nanospheres (Graetsch, 1994). We can use the ratio of the intensities of the broad band at 3680 cm^{-1} (I_{3680}) and the prominent band at 1055 cm^{-1} for $v3$ SiO_4^{4-} (I_{1055}) to express the change in the amount of weakly bonded H_2O groups and Si–OH groups in the silica glaze. Here, the intensities of the bands were calculated by subtracting an average background from the corresponding peak height. The ratio between these calculated intensities increases from

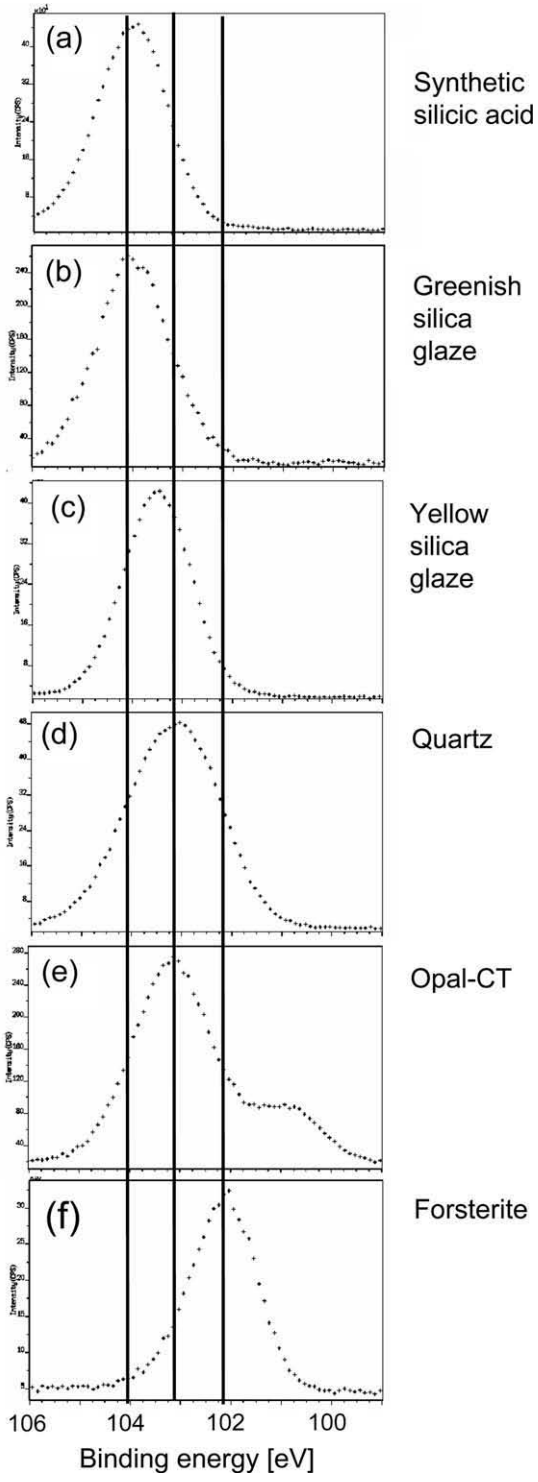

Fig. 7. Si 2p spectra for various silicate minerals, silicic acid and the silica glazes from Nopal; solid lines indicate the locations of the maxima in the spectra for forsterite, opal-CT, and silicic acid.

$I_{3680}/I_{1055} = 0.010(5)$ for the yellow silica glaze to $I_{3680}/I_{1055} = 0.030(5)$ for the greenish silica glaze, in accord with the shift of the Si 2p peak in the corresponding XPS-spectra, which also indicates a higher number of Si–OH groups on the surface of the nanospheres in the greenish silica glaze (see Fig. 8).

3.6. $\delta^{18}O$ in the silica glaze

Stable-isotope measurement using a secondary-ion mass spectrometer gave an average $\delta^{18}O$ value of $26.5 \pm 1.1‰$ for the yellow silica glaze and $21.2 \pm 1.1‰$ for the green silica glaze of the outer rim. The $\delta^{18}O$ value of the yellow coating agrees with a previously reported $\delta^{18}O$ value for silica glaze of ~26‰ by Calas et al. (2008). Assuming a meteoric fluid composition of $\delta^{18}O = -8‰$, the authors calculated a temperature of formation of 29 °C for the yellow opal using the fractionation values of Kita et al. (1985). Assuming a similar meteoric fluid composition, the lower $\delta^{18}O$ value of the green silica glaze indicates either a higher temperature of formation (51 °C) or a higher water/rock ratio relative to the conditions of formation of the yellow silica glaze. Isotope measurements on yellow opal from the high-grade site resulted in extreme variations in the $\delta^{18}O$ value (4.6–34‰), most likely the results of small inclusions of weeksite and uraninite inside the silica glaze.

4. DISCUSSION

Examination of the yellow and greenish silica glazes with various analytical methods showed the occurrence of U-bearing species and particles in the silica glazes, which contain less Fe, Al, K, Na, Mg, Ti than the underlying rock.

4.1. Mineral particles in the silica glazes

The presence of microparticles of uraninite and uranylsilicates in the outer parts of all silica glazes are the result of the properties of amorphous silica prior to its hardening to opal A. Freshly precipitated amorphous silica is a gel-like material with a lower viscosity than secondary phases such as iron-hydroxides and clays. As a result, the gel can entomb particles during its gelation and condensation. Perry et al. (2006) argued that this silica-binding character explains the incorporation of detrital grains, organics, and

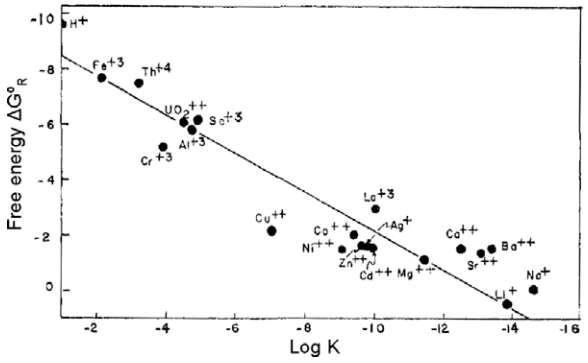

Fig. 8. Plot (modified from Dugger et al. (1964)) of log K for the reaction $M^{z+} + (\text{–Si–OH}) = \text{Si–O–M} + H^+$ versus the normalized free energy (ΔG) for the reaction $M^{z+} + \text{Si–O–} = \text{Si–O–}M$ (M = undefined cation).

aerosols from local environments into silica glazes (silica glazes) and coatings composed of opal, clays, organics, manganese, and iron oxides (desert varnish).

4.2. Chemical composition and conditions of formation of the silica glazes

The silica glazes from Nopal I contain low concentrations of Al, K, Na, Fe, S, P, and $(CO_3)^{2-}$ relative to Si, Ca, U, and S. These lower concentrations relative to Si are common in colourless, clear and translucent silica glazes (Dorn, 1998). To understand the absence of clays, iron-hydroxides or carbonates in the silica glazes, Curtiss et al. (1985) modeled the formation of Si-rich coatings in the arid zones of Hawaii using data from dissolution experiments of local windborne material to calculate the proportions of phases that would form during evaporation of water films on rock surfaces. They showed that prior to the formation of carbonates and sulfates, amorphous silica is the predominant product of the evaporation process, followed by minor amounts of kaolinite and hematite. Calculated amounts of hematite in the precipitate were higher than the observed amounts of iron oxides in the coatings. This was explained by precipitation of the latter minerals on non-dissolved mineral grains and subsequent removal of these grains during strong rainfall events. Other dissolved species in the water film, such as alkaline and alkaline-earth cations and sulfate and carbonate ions, precipitate as soluble sulfates and carbonates on top of the amorphous silica coatings. Curtiss et al. (1985) explained their absence in the silica glazes from Hawaii by dissolution of these phases during strong rainfall events.

The model of Curtiss et al. (1985) explains the absence of clays and iron-hydroxide within colourless silica glazes. However, the source of silica for the glazes from the Nopal I uranium deposit must not be exclusively windborne. Pore and surface water dissolving the welded tuff at higher levels percolated downward and deposited some of the silica on the surfaces of the exposed rocks. However, the absence of opaline coatings in deeper parts of the vadose zone (fractures and cracks) suggests that most of the silica originates from fine particles dissolved on surface of exposed rocks. Here, potential windborne particles at the U ore deposit most likely originate from (a) breccia and tuff, (b) minerals of the ore body (uraninite and pyrite), (c) uranyl minerals (e.g. uranophane, weeksite), and (d) secondary minerals inside the breccia pipe: sulfates (e.g. jarosite, gypsum), silicates (e.g. kaolinite), and Fe-oxides (e.g. hematite). The proximity of the collected coatings to breccia, tuff, and uranyl minerals suggests that partial dissolution of windborne particles from these sources significantly contributed to the formation of silica glaze. For example, the occurrence of fissures filled with becquerelite between the silica glazes and layers of uranyl-silicates indicate dissolution of the latter minerals and subsequent precipitation of becquerelite at an earlier stage of silica glaze formation. Hence, dissolved species in the water film prior to the precipitation of colloidal silica originated from the dissolution of windborne particles (uranyl-silicates, tuff, breccia). Consideration of the latter material as a source for silicic acid in the water film could explain the occurrence of silica glazes on uranophane-β single crystals (Cesbron et al., 1993). Here, the coatings mimic the prismatic morphology of the uranophane-β crystals, the result of dissolution–precipitation in a thin water film covering the entire external surface of each crystal.

The low concentrations of Al, K, Na, Fe, S, P, and $(CO_3)^{2-}$ with respect to Ca and U in the silica glazes must be attributed to (a) the higher proportion of the latter elements in solution, and (b) removal of clay and iron-hydroxide particles prior to hardening of the opal (see above). The observed Ca:U ratio of 1:1 suggests trapping of either Ca-(UO_2)-bearing aqueous species or particles within the colloidal silica. Zellerite, $Ca[UO_2(CO_3)](H_2O)_5$ and metazellerite, $Ca[UO_2(CO_3)](H_2O)_3$ are the only known minerals, which contain Ca and U as the only cationic species in a ratio of 1:1. Other minerals with Ca:$(UO_2)^{2+}$ ratios of 1:1 are Cu-, Na-, and Mg-bearing minerals, namely ulrichite, $Cu(H_2O)_4[Ca(UO_2)(PO_4)_2]$, swarzite, $CaMg(H_2O)_{12}[(UO_2)(CO_3)_3]$, and andersonite, $Na_2Ca[(UO_2)(CO_3)_3](H_2O)_5$ (Burns, 2005). These examples show that one cannot rule out the trapping of nanoparticles of an uranyl-carbonate or uranyl-hydroxy-hydrate with a Ca:$(UO_2)^{2+}$ ratio of 1:1. Note that the occurrence of $(CO_3)^{2-}$ in the colloidal silica coatings cannot be ruled out completely because (a) vibration bands of $(CO_3)^{2-}$ groups in IR spectra can overlap with bands for $(SiO_4)^{4-}$, H_2O, and $(UO_2)^{2+}$ (Cejka, 1999), and (b) the low sensitivity factor of C limits the detection of $(CO_3)^{2-}$ groups in C 1s spectra to samples of high $(CO_3)^{2-}$ concentration.

4.3. Incorporation of U and Ca aqueous species into colloidal silica

To understand the possible incorporation of a Ca-U-{O/OH/H_2O/$(CO_3)^{2-}$} aqueous species into the colloidal silica, one must examine the stability of complexes of Si–O polymers and Ca and U. Colloidal silica has a high surface area (>400 $m^2\ g^{-1}$, Goworek, 2000), promoting low diffusion of ionic species through its water-filled pores. This property of colloidal silica is used in growth experiments of single crystals, where the slow diffusion of ionic species limits the number of seed crystals (Henisch, 2005), and in the containment of ionic species in contaminated sites where colloidal silica is used as a barrier material (Hakem et al., 2004).

Dugger et al. (1964) examined the adsorption of cations on terminal silanol groups in colloidal silica. The sorption process of a cation M can be described as

$$M^{z+} + (\text{–Si–OH}) = \text{Si–O–M} + H^+ \quad (1)$$

Reaction (1) is the sum of the two reactions:

$$\text{Si–OH} = \text{Si–O}^- + H^+ \quad (2)$$

$$M^{z+} + \text{Si–O}^- = \text{Si–O–}M \quad (3)$$

Fig. 8 shows the variation of log K for Eq. (1) as a function of the normalized free energy of reaction (3) (for details see Dugger et al., 1964). It is apparent that terminal $Si–O^-$ species have a high affinity to sorb high-strength cations such as UO_2^{2+}. This property can be explained with bond-valence theory (Brown, 2002) and its application to

the adsorption of cations on mineral surfaces (e.g. Schindler et al., 2009c). The Si–O^- surface termination is a strong Lewis base, which forms a stable bond with strong Lewis acids such as UO_2^{2+}, Fe^{3+}, Al, etc. Considering these properties of colloidal silica, the strong Lewis acid $(UO_2)^{2+}$ forms stronger complexes with Si–O polymers and diffuses more slowly through the colloidal silica than the weaker Lewis acid Ca^{2+}. Hence, diffusion of the species $(UO_2)^{2+}$ and Ca^{2+} into colloidal silica or the trapping of Ca^{2+}- and $(UO_2)^{2+}$-species with colloidal silica are unlikely to result in a ratio of 1:1 in the different zones of the silica glazes.

4.4. Aqueous species with a Ca:U ratio of 1:1

Another possibility for incorporating Ca and U would be the trapping or diffusion of an aqueous species with a Ca:U ratio of 1:1 into colloidal silica. To our knowledge, there has been no spectroscopic study on the occurrence of aqueous species in the Ca–U–Si system for solutions supersaturated with respect to amorphous silica. However, studies on the speciation of U in calcite-equilibrated solutions showed the presence of a $Ca_2UO_2(CO_3)_3$ aqueous species (Bernhard et al., 1996, 2001), indicating that Ca–U aqueous species do occur in certain natural environments. We showed above that during the earlier stage of silica-gel formation, becquerelite precipitates as a result of the dissolution of uranophane and weeksite. The precipitation of becquerelite indicates the co-existence of a Ca–U-enriched solution with amorphous silica. Hence, the occurrence of an Ca–U aqueous species and its trapping in the colloidal silica could be an alternative mechanism to the incorporation of Ca–U particles and could explain the Ca:U ratio of 1:1 in the different zones of the silica glazes.

4.5. Conditions of formation of the silica glazes

4.5.1. A. Moisture content

The relatively constant $\delta^{18}O$ values in the different zones of the green and yellow silica glazes from the breccia pipe indicate that conditions such as temperature and moisture did not change during formation of the coatings. The greenish silica glaze was sampled proximal to a fault where the volcanic rocks are more highly brecciated than in the center of the ore body. As a consequence of this intense brecciation, the rocks have higher permeability and allow enhanced percolation of meteoric water (with a $\delta^{18}O$ value of $\langle -8‰ \rangle$) relative to the breccia in the center of the pipe. Hence, the lower $\delta^{18}O$ values of the greenish silica glazes suggest a more water-dominated system (i.e. higher moisture content) relative to the conditions of formation of the yellow silica glaze.

The green silica glazes are on average twice as thick as the yellow silica glazes from the center of the breccia (see above). The greater thickness of the green coating may also be the result of a higher moisture content during its formation, because an increase in the latter content results in an increase in the dissolution rate of windborne particles on the surface of rocks and minerals. Curtiss et al. (1985) draw a similar conclusion when they compared the thickness of silica glazes from areas of higher and lower precipitation on Hawaii. The higher moisture contents around the fault may also be the reason for a higher proportion of terminal Si–OH groups and molecular water in the green coating, as higher moisture in the proximity of amorphous silica can slow down its dehydration in an arid or semi-arid environment.

4.5.2. B. Eh conditions

The XPS-measurements indicate U^{6+}:U^{4+} ratios in the range 54:46 to 68:32 on the surfaces of the silica glazes and hematite coatings (Table 1). Although XPS is a surface analytical method, it is reasonable to assume that the lower-valence cation U^{4+} occurs in similar or even higher proportions inside the coatings. We are confident that the ratios of U^{6+}:U^{4+} in the U 4f spectra for hematite, and the yellow and greenish silica glazes reflect the redox potentials (Eh) during formation of the coatings.

We described above the higher amount of water percolating through pores and fissures of the breccia closer to the fault. As a consequence, the breccia in this region shows a higher degree of weathering and oxidation than the breccia in the center of the pipe (Figs. 1b and 2b). The corresponding increase in Eh from the center of the pipe toward the fault is reflected in the increase in the U^{6+}:U^{4+} ratio from 54:46 to 68:32 from the yellow to the greenish silica glaze.

4.6. The internal structure of the silica glazes

The internal structure of sintered silica reflects the mechanism of coalescence of the silica nanospheres during dehydration of the colloidal silica. In a diffusion-limited aggregation of nanoparticles, the contact regions between the nanospheres gain local curvature, and strings of peanut-shaped units or spherical particles are generated (VanDamme, 2000).

Variable concentrations of U and Ca inside the silica glazes illustrate their internal structure (Fig. 4). Local curvatures and spherical particles of silica occur in all zones, and indicate trapping of Ca_1U_1 species or particles with different generations of colloidal silica, followed by the formation of curves and spheres during dehydration. Closer inspection of the zonation of U in the silica glazes shows the occurrence of spherical features in the yellow coatings and curved-layered features in the greenish coating (Figs. 4b, c, and e). Spherical features display a higher degree of curvature than curved-layered features. If we assume that the degree of curvature in the silica glazes correlates with the aggregation state of the nanoparticles, then the particles in the yellow coating occur in a more advanced aggregation state. This state may be related to the dehydration of the silica glaze and would explain the lower amount of Si–OH groups in the yellow coating relative to the green coating.

4.7. Retardation of U and organic components by Si-rich coatings

We showed above that all silica glazes contain U^{4+} species, although the greenish glaze occurs in a moist oxidative environment. Furthermore, the occurrence of the curved

and spherical zones of U (formed during hardening of the colloidal silica) indicates that U was not leached from the silica glazes after their formation. These observations suggest that silica glazes and opaline coatings of the subsurface are able to (a) protect reduced radionuclides from oxidation, and (b) prevent their mobilization over time.

Perry and Kolb (2003) and Perry et al. (2004) showed that Si-rich rock coatings (Si-rich desert varnish) contain amino acids and DNA, and Perry et al. (2003, 2006) discussed a possible binding mechanism of colloidal silica with respect to those organic constituents. This work and our studies show that Si-rich rock coatings are able to preserve organic and inorganic components from the atmosphere, important aspects not only with respect to the retardation of radionuclides but also in terms of gaining paleohydrologic, palaeobiologic, and palaeoenvironmental information.

4.8. Can opaline coatings retard radionuclides over geological time-scales?

Dorn (1998) pointed out that silica glazes are unstable over a time frame of thousands of years. He showed that silica glazes have many internal fractures, which promote detachment of the coatings from the rock. Moreover, they are susceptible to biochemical erosion. However, opaline coatings in fractures and cavities at the subsurface are less exposed to such erosion. For example, Paces et al. (2004) showed that the age of finely laminated opals in the fractures of the welded tuffs at Yucca Mountain range from 40 to 700 ka. These ages indicate that opaline coatings in the subsurface of a semi-arid environment are quite stable and that retardation of radionuclides by opaline coatings may occur over this timeframe.

5. SUMMARY

Examination of silica glazes from the uranium ore deposit at Peña Blanca showed that

(a) the glazes are strongly zoned with respect to Ca and U;
(b) Ca and U occur in the ratio of 1:1, most likely the result of the trapping of Ca_1U_1-particles or aqueous species by colloidal silica;
(c) microparticles of weeksite and uraninite have been incorporated into the glazes during gelation and hardening of silicic acid to opal;
(d) the U^{6+}:U^{4+} ratios in the glazes reflect the change in Eh conditions from the center of the breccia pipe toward the fault;
(e) the lower $\delta^{18}O$ value and the higher proportion of Si–OH terminal groups in the glazes reflect the change in moisture content from the center of the breccia pipe toward the fault;
(f) opals formed as fillings in fractures in close proximity to a potential nuclear waste repository may retard radionuclides in a time frame of 40 to 700 ka.

ACKNOWLEDGEMENTS

This work was supported by Discovery Grants to M.S., M.F., and F.C.H. from the Natural Sciences and Engineering Research Council of Canada, Canada Research Chairs to M.F. and F.C.H., and C.F.I. grants to F.C.H. We thank Aaron Lussier and Neil Ball for help on the IR spectrometer and Panseok Yang for help on the electron microprobe. We are indebted to Michael Freund for the use of the XPS spectrometer in his laboratory at the University of Manitoba. We also thank three anonymous reviewers and Associate editor Dr. Johnson Haas for their comments on an earlier version of the paper.

REFERENCES

Brown I. D. (2002) *The Chemical Bond in Inorganic Chemistry. The Bond-Valence Model*. Oxford University Press, 2002.

Bernhard G., Geipel G., Brendler V. and Nitsche H. (1996) Speciation of uranium in seepage waters of a mine tailing pile studies by time-resolved laser-induced fluorescence (TRFLS). *Radiochim. Acta* **74**, 87–91.

Bernhard G., Geipel G., Reich T., Brendler V., Amayri S. and Nitsche H. (2001) Uranyl(VI) carbonate complex formation: validation of the $Ca_2UO_2(CO_3)_3$(aq.) species. *Radiochim. Acta* **89**, 511–518.

Burns P. C. (2005) U^{6+} Minerals and inorganic compounds: insights into an expanded structural hierarchy of crystal structures. *Can. Mineral.* **43**, 1839–1894.

Calas G. (1977) Les phenomenes d'alteration hydrothermale et leur relation avec les mineralisations uraniferes en milieu volcanique: Le cas des ignimbrites tertiaires de la Sierre Pena Blanca, Chihuahua, Mexico. *Sci. Geol. Bull.* **30**, 3–18.

Calas G., Agrinier P., Allard T. and Ildefonse P. (2008) Alteration geochemistry of the Nopal I uranium deposit (Sierra Pena Blanca, Mexico), a natural analogue for a radioactive waste repository in volcanic tuffs. *Terra Nova* **20**, 206–212.

Cejka J. (1999) Infrared spectroscopy and thermal analysis of the uranyl minerals. *Rev. Mineral.* **38**, 521–622.

Cesbron F., Ildefonse P. and Sichere M. C. (1993) New mineralogical data on uranophane and β-uranophane; synthesis of uranophane. *Mineral. Mag.* **57**, 301–308.

Curtiss B., Adams J. B. and Ghiorso M. S. (1985) Origin, development and chemistry of silica–alumina rock coatings from the semi-arid regions of the islands of Hawaii. *Geochim. Cosmochim.* **49**, 49–56.

Dobson P. F., Kneafsey T. L., Sonnenthal E. L., Spycher N. and Apps J. A. (2003) Experimental and numerical simulation of dissolution and precipitation: implications for fracture sealing at Yucca Mountain, Nevada. *J. Contam. Hydrol.* **62–63**, 459–476.

Dobson P., Fayek M., Goodell P., Ghezzehel T., Melchor F., Murell M., Oliver R., Reyes-Cortés I., de la Garza R. and Simmons A. (2008) Stratigraphy of the PB-1 well, Nopal I Uranium Deposit, Sierra Peña Blanca, Chichuahua, Mexico. *Int. Geol. Rev.* **50**, 1–16.

Dorn R. I. (1998) *Rock Coatings*. Amsterdam, Elsevier, 429 p.

Dugger D. L., Stanton J. H., Irby B. N., McConell B. L., Cummings W. W. and Maatman R. W. (1964) The exchange of twenty metal ions with the weakly acidic silanol group of silica gel. *J. Phys. Chem.* **68**, 757–760.

Ewing R. C. and van Hippel F. N. (2009) Nuclear waste management in the United States-starting over. *Science* **325**, 151–152.

Fayek M., Ren M., Goodell P., Dobson P., Saucedo A. L., Kelts A., Utsunomiya S., Ewing R. C., Riciputi L. R. and Reyes I.

(2006) Paragenesis and geochronology of the Nopal I uranium deposit, Mexico. In *2006 International High Level Radioactive Waste Management Conference Proceedings*, Las Vegas, Nevada, April 30–May 4, CD-ROM.

Goworek J. (2000) Thermogravimetric approach for determining porosity of colloidal silicas. In *Adsorption of Silica Surfaces* (ed. E. Papirer). Marcel Dekker, New York.

Graetsch H. (1994) Structural characteristics of opaline and microcrystalline silica minerals. *Rev. Mineral.* **29**, 209–229.

Hakem N., Apps J. A., Moridis G. J. and Mahamid I. A. I. (2004) Sorption of fission product radionuclides, ^{137}Cs and ^{90}Sr, by Savannah River Site sediments impregnated with colloidal silica. *Radiochim. Acta* **92**, 419–432.

Henisch H. K. (2005) *Crystals in Gels and Liesegang Rings*. Cambridge University Press, p. 212.

Herdianita N. R., Rodgers K. A. and Browne R. L. (2000) Routine instrumental procedures to characterize the mineralogy of modern and ancient sinters. *Geothermics* **29**, 65–81.

Ildefonse P., Muller J. P., Clozel B. and Calas G. (1990) Study of two alteration systems as natural analogues for radionuclide release and migration. *Eng. Geol.* **29**, 413–439.

Kita I., Taguchi S. and Matsubaya O. (1985) Oxygen isotope fractionation between amorphous silica and water at 34–93 °C. *Nature* **314**, 83–84.

Long J. C. S. and Ewing R. C. (2004) Yucca Mountain: earth science issues at a geologic repository for high-level nuclear waste. *Ann. Rev. Earth Planet. Sci.* **32**, 363–401.

Lynne B. Y. and Campbell K. A. (2004) Morphologic and mineralogic transitions from opal-A to opal-CT in low-temperature siliceous sinter diagenesis, Taupo volcanic zone, New Zealand. *J. Sediment. Res.* **74**, 561–579.

Lynne B. Y., Campbell K. A., Moore J. N. and Borne P. R. L. (2005) Diagenesis of 1900-year old siliceous sinter (opal A to quartz) at Opal Mound, Roosevelt Hot Springs, Utah, U.S.. *Sedimen. Geol.* **119**, 249–278.

Michard P. M., Guibel E., Vincent T. and Le Cloirec P. (1996) Sorption and desorption or uranyl ions by silica gel: pH, particle size and porosity effects. *Microporous Mater.* **5**, 309–324.

Macfarlane A. M. and Ewing R. C. (2006) *Uncertainty Underground-Yucca Mountain and the Nation's High-Level Nuclear Waste*. MIT Press, Cambridge, MA, 431 p.

Moll H., Geipel G., Brendler V. and Nitsche B. H. (1998) Interactions of uranium(VI) with silicic acid in aqueous solutions studied by time-resolved laser-induced fluorescence spectroscopy (TRLFS). *J. Alloys Comp.* **271–273**, 765–768.

Murphy W. M. (2000) Natural analogs and performance assessment for geologic disposal of nuclear waste. *Mater. Res. Soc. Symp. Proc.* **608**, 533–544.

Muller J. P., Ildefonse P. and Calas G. (1990) Paramagnetic defect centers in hydrothermal kaolinite from an altered tuff, (Nopal uranium deposit, Chihuahua, Mexico). *Clays Clay Miner.* **38**, 600–608.

Paces J. B., Neymark L. A., Marshall B. D., Whelan J. F. and Peterman Z. E. (2001) Ages and origins of calcite and opal in the exploratory studies facility tunnel, Yucca Mountain, Nevada. *US Geol. Surv. Water-Resour. Invest. Rep.* 01-4049.

Paces J. B., Newmark L. A., Wodden J. L. and Persing H. M. (2004) Improved spatial resolution for U-series dating of opal at Yucca Mountain, Nevada, USA, using ion-microprobe and microdigestion methods. *Geochim. Cosmochim.* **68**, 1591–1606.

Pearcy E. C., Prikryl J. D., Murphy W. M. and Leslie B. W. (1994a) Alteration of uraninite from the Nopal I deposit, Peña Blanca district, Chihuahua, Mexico, compared to degradation of spent nuclear fuel in the proposed US high-level nuclear waste repository at Yucca Mountain, Nevada. *Appl. Geochem.* **9**, 713–732.

Pearcy E. C., Prikryl J. D., Murphy W. M. and Leslie B. W. (1994b) Alteration of uraninite from the Nopal I deposit, Pena Blanca district, Chihuahua, Mexico, compared to degradation of spent nuclear fuel in the proposed US high-level nuclear waste repository at Yucca Mountain, Nevada. *Appl. Geochem.* **9**, 713–732.

Pearcy E. C., Prikryl J. D. and Leslie B. W. (1995) Uranium transport fractured silicic tuff and relative retention in areas with distinct fracture characteristics. *Appl. Geochem.* **10**, 685–704.

Petit J. C. (1990) Migration of radionuclides in the geosphere: what can we learn about natural analogs? *Radiochim. Acta* **51**, 181–188.

Perry R. S., Lynne B. Y., Sephton M. A., Kolb V. M., Perry C. C. and Staley J. T. (2006) Baking black opal in the desert sun: the importance of silica in desert varnish. *Geology* **34**, 537–540.

Perry R. S. and Kolb V. M. (2003) Biological and organic constituents of desert varnish: review and hypotheses. In *Instruments, methods and missions for Astrobiology VII: bellingsham* (eds. R. B. Hoover and A. Y. Rozanov). SPIE, Washington, v.5163, pp. 202–217.

Perry R. S., Engel M. H., Botta O. and Staley J. T. (2003) Amino acid analyses of desert varnish from the Sonoran and Mojave Deserts. *Geomicrobiol. J.* **20**, 427–438.

Perry R. S., Dodsworth J., Staley J. T. and Engel M. H. (2004) Bacterial diversity in desert varnish: Third European Workshop on Exo/Astrobiology, Mars: The search for life. The Netherlands, European Space Agency Publications, v. SP-545, pp. 55–58.

Pouchou J. L. and Pichoir F. (1985) "PAP" φ(rZ) procedure for improved quantitative microanalysis. *Microbeam Anal.* **1985**, 104–106.

Prikryl J. D., Pickett D. A., Murphy W. M. and Pearcy E. C. (1997) Migration behavior of naturally occurring radionuclides at the Noal I uranium deposit, Chihuahua, Mexico. *J. Contam. Hydrol.* **26**, 61–69.

Reeder R. J., Nugent M., Tait C. D., Morris D. E., Heald S. M., Beck K. M., Hess W. P. and Lanzirotti A. (2001) Coprecipitation of uranium(VI) with calcite: XAFS, micro-XAS, and luminescence characterization. *Geochim. Cosmochim. Acta* **65**, 3491–3503.

Reich T., Moll H., Arnold T., Denecke M. A., Hennig C., Geipel G., Bernhard G., Nitsche H., Allen P. G., Bucher J. J., Edelstein N. M. and Shuh D. K. (1998) An EXAFS study of uranium(VI) sorption onto silica gel and ferrihydrite. *J. Electron Spectrosc. Relat. Phenom.* **96**, 237–243.

Schindler M., Hawthorne F. C., Putnis C. and Putnis A. (2004) Growth of uranyl-hydroxy-hydrate and uranyl-carbonate minerals on the (1 0 4) calcite surface. *Can. Mineral.* **42**, 1683–1697.

Schindler M., Freund M., Hawthorne F. C. and Burns P. C. (2009a) XPS spectra of uranyl minerals and synthetics. I. The U 4f Spectrum. *Geochim. Cosmochim.* **73**, 2471–2487.

Schindler M., Freund M., Hawthorne F. C. and Burns P. C. (2009b) XPS spectra of uranyl minerals and synthetics. II. The O 1s Spectrum. *Geochim. Cosmochim.* **73**, 2488–2509.

Schindler M., Freund M., Hawthorne F. C., Burns P. C. and Maurice P. A. (2009c) Dissolution of uranophane-alpha: an AFM, XPS and SEM study. *Geochim. Cosmochim. Acta* **73**, 2510–2533.

Shirley D. A. (1972) High-resolution X-ray photoemission spectrum of the valence bands of gold. *Phys. Rev.* **B5**, 4709–4714.

Smith D. K. (1998) Opal, christobalite and tridymite, Noncrystallinity versus crystallinity. Nomenclature of the silica minerals and bibliography. *Powder Diffraction* **13**, 2–19.

Szabo B. J. and Kyser T. K. (1990) Ages and stable isotope compositions of secondary calcite and opal in drill cores from Tertiary volcanic rocks of the Yucca Mountain area, Nevada. *Geol. Soc. Am. Bull.* **102**, 1714–1719.

Thiagarajan N. and Lee C. T. A. (2004) Trace-element evidence for the origin of desert varnish by direct atmospheric deposition. *Earth Planet. Sci. Lett.* **224**, 131–141.

Vision 2.2.6 (2006) Kratos Analytical Ltd.

VanDamme H. (2000) Nanoscale and mesoscale morphology of silica surfaces. In *Absorption on Silica Surfaces: Surfactant Science Series* (ed. U. Papirer). Marcel Dekker, Ney York, pp. 119–166.

Vochten R., Blaton N. and Peeters O. (1997) Synthesis of sodium weeksite and its transformation into Weeksite. *Neues Jb. Miner. Mh.* **12**, 569–576.

Wagner C. D., Riggs W. M., Davis L. E., Moulder J. F. and Mailenberg G. M. (1979) *Handbook of X-ray Photoelectron Spectroscopy*. Perkin-Elmer.

Whelan J. F., Paces J. B. and Peterman Z. E. (2002) Physical and stable-isotope evidence form formation of secondary calcite and silica in the unsaturated zone, Yucca Mountain, Nevada. *Appl. Geochem.* **17**, 735–750.

Associate editor: Johnson R. Haas